nature communications

Article

https://doi.org/10.1038/s41467-025-58639-z

Metal-organic framework glass stabilizes high-voltage cathodes for efficient lithium-metal batteries

Received: 4 January 2025

Accepted: 26 March 2025

Published online: 12 April 2025

Check for updates

Lishun Bai[1,3], Yan Xu[1,3], Yue Liu[1], Danni Zhang[1], Shibin Zhang[1], Wujie Yang[2], Zhi Chang[1] ✉ & Haoshen Zhou[2] ✉

The rapid evolution of portable electronics and electric vehicles necessitates batteries with high energy density, robust cycling stability, and fast charging capabilities. High-voltage cathodes, like $LiNi_{0.8}Co_{0.1}Mn_{0.1}O_2$ (NCM-811), promise enhanced energy density but are hampered by poor stability and sluggish lithium-ion diffusion in conventional electrolytes. We introduce a metal-organic framework (MOF) liquid-infusion technique to fully integrate MOF liquid into the grain boundaries of NCM-811, creating a thoroughly coated cathode with a thin, rigid MOF Glass layer. The surface electrically non-conductive MOF Glass layer with 2.9 Å pore windows facilitating Li-ion pre-desolvation and enabling highly aggregative electrolyte formation inside the Glass channels, suppressing solvated Li-ion co-insertion and solvent decomposition. While the inner Glass layer composes of Li-ion conducting components and enhancing fast Li-ion diffusion. This functional structure effectively shields the cathode from particle cracking, CEI rupture, oxygen loss, and transition metal migration. As a result, Li||Glass@NCM-811 cells demonstrate good rate capability and cycling stability even under high-charge rates and elevated voltages. Furthermore, we also achieve a 385 Wh kg^{-1} pouch-cell (19.579 g, for pouch-cell), showcasing the practical potential of this method. This straightforward and versatile strategy can be applied to other high-voltage cathodes like Li-rich manganese oxides and $LiCoO_2$.

The proliferation of various electronic devices and electric vehicles (EVs) eagerly calls for batteries with high energy density, long cycle life, and excellent fast-charging performance[1,2]. Cathode materials with high specific capacities and high voltage are essential for constructing batteries with high energy density and long cycle life properties[3–5]. However, those high-voltage and high-capacity cathode materials usually suffered from poor stability and slow lithium-ion diffusion when coupled with electrolyte, which make it difficult to construct batteries with high energy density, long cycle life, and fast-charging properties[6–9]. Take $LiNi_xCo_yMn_{1-x-y}O_2$ (NCM) as an example: during electrochemical cycles, NCM cathodes undergo various detrimental processes, including significant phase transformations, extensive cracking along grain boundaries of secondary particles, continuous rupture of cathode electrolyte interphases (CEIs), and violent side reactions induced by constant electrolyte decomposition (accelerated by catalytic NCM cathode)[10–12]. Those annoying detrimental problems are closely related to the co-insertion of solvated Li-ion/solvent into the structure of cathodes, consequently lead to the generation of gases

[1]School of Materials Science and Engineering, Key Laboratory of Electronic Packaging and Advanced Functional Materials of Hunan Province, Central South University, Changsha 410083 Hunan, China. [2]Center of Energy Storage Materials & Technology, College of Engineering and Applied Sciences, National Laboratory of Solid State Micro-structures, Nanjing University, Nanjing 210093, PR China. [3]These authors contributed equally: Lishun Bai, Yan Xu.
✉e-mail: zhichang@csu.edu.cn; hszhou@nju.edu.cn

(oxygen, carbon dioxide etc.) and transition metals (TM) dissolution and migration[13–15]. It is important to note that the migration of TM to the anode and the production of gases can severely degrade the anode and pose significant safety concerns[16–18]. Even worse, these issues become more severe when electrolytes penetrate the interior of secondary cathode particles, accelerating particle cracks, CEI rupture, gases production, and transition metal dissolution/migration, ultimately leading to premature cell failure and potential safety hazards[11,12,19,20].

Significant research efforts have been made to stabilize high-voltage cathodes, including heterogeneous element doping[21,22], structural engineering[23–27], electrolyte modification[8,28–31], and surface coating[32,33]. Among these strategies, surface coating is considered the simplest yet most effective method for markedly improving the stability of high-voltage cathodes. By constructing highly stable and catalytically inert coating layer on cathode surfaces, those aforementioned detrimental issues induced by the co-insertion of solvated Li-ion/solvent can be effectively addressed[34–36]. However, several inherent defects significantly counteract the positive effects of surface coating strategies for high-voltage cathodes. First, achieving complete coating coverage is still challenging[37]. Most coatings remain only on the surface of secondary cathode particles, making it difficult to penetrate and coat the interiors and grain boundaries of primary particles[38]. Second, many coating processes are complex, time/energy-consuming, and conducted in solutions, which may adversely affect the stability of the cathode materials[37]. Additionally, the introduction of a common type of coating layer may impedes lithium-ion transport to some extent, which is detrimental to the rate performance of the cathode materials. Lastly, although most coatings can partially block direct contact between the electrolyte and cathode particles, they often have large gaps which typically larger than solvated lithium ions[38]. This limitation makes it difficult to fundamentally inhibit electrolyte penetration, thus failing to effectively prevent electrolyte decomposition and the co-intercalation of solvated lithium ions into the cathode materials[32]. Optimized coating strategies have been developed to address these issues, yet few can simultaneously resolve all the aforementioned limitations. Therefore, it is highly desirable to develop a simple but effective coating strategy to address those limitations simultaneously.

In this work, we present a straightforward metal-organic framework (MOF, Zn-P-dmbIm) liquid-infusion strategy for high-voltage cathodes like ($LiNi_{0.8}Co_{0.1}Mn_{0.1}O_2$/NCM-811). The process involves heating MOF powder to 175 °C, transforming it into a flowable MOF liquid that thoroughly infuses into the inner primary cathode particles before rapid cooling to room temperature. This process ensures the MOF Glass thoroughly coats both the grain boundaries and the surfaces of the primary NCM-811 particles, achieving complete (100%) MOF Glass coverage (Glass@NCM-811). This strategy significantly outperforms conventional coating techniques by forming a unique double-layer structure: the surface electrically non-conductive MOF Glass layer with 2.9 Å pore windows facilitating Li-ion pre-desolvation and enabling highly aggregative electrolyte formation inside the Glass channels, suppressing solvated Li-ion co-insertion and solvent decomposition. The inner Glass layer consists of Li-ion conductive components, which significantly enhance fast Li-ion diffusion. This Glass coating shields the NCM-811 cathodes from particle cracks, CEI rupture, gas generation, and transition metal dissolution/migration while demonstrating fast Li-ion diffusion (Fig. 1a, b). Consequently, Li||Glass@NCM-811 cells demonstrate good rate capability and cycling stability, even under harsh conditions of high charge rates (5 C) and elevated voltages (4.6 V). The versatility of this MOF Glass coating strategy can also be extended to other high-voltage cathodes, such as Li-rich manganese oxides (LRMO) and $LiCoO_2$ (LCO). The practical application of this strategy is evidenced by a 385 Wh kg^{-1} pouch-cell assembled with Glass@NCM-811, showcasing its effectiveness and potential for advancing high-energy-density batteries.

Results and discussion

MOF liquid-infusion preparing MOF Glass infused high-voltage cathode

In their previous studies, researchers demonstrated that coating electrode surfaces with porous materials featuring sub-nanochannels can facilitate the pre-desolvation of Li-ions[39–41]. This approach effectively suppresses electrolyte decomposition and prevents the co-intercalation of solvated Li-ions into electrode materials. Yet, these benefits were achieved only on electrode level as the porous materials were directly coated on the electrode surface, which means it cannot achieve real particle-level Li-ions pre-desolvation[42]. However, attempts to thoroughly mix cathodes with porous materials like metal-organic frameworks (MOFs) face significant challenges. Due to the powdery nature of MOFs, achieving comprehensive and uniform coverage of the cathode particles is difficult. Furthermore, this method only coats the surface of secondary particles, leaving the inner primary particles uncoated, thus failing to ensure complete coverage[38]. Additionally, the introduction of a coating layer can often impede lithium-ion transport to some extent, which can negatively impact the rate performance of the cathode materials. Complex and time-consuming liquid phase methods, which involve water or other solvents to coat cathodes with MOFs, introduce further complications. These processes can adversely affect the stability of the cathodes due to the presence of additional solvents.

To achieve effective Li-ion pre-desolvation, the pore windows of porous materials should be smaller than the size of solvated Li-ions, which is approximately 7.0 Å[42,43]. Ideally, the porous coating material should also be capable of transforming into a flowing liquid state. This allows the liquid MOF to diffuse into the inner voids of the secondary cathode particles and infuse into the grain boundaries between the primary cathode particles, thus ensuring 100% MOF coverage. Taking into account the above two prerequisites, a unique MOF namely Zn-P-dmbIm comes into our consideration (Supplementary Fig. 1)[44]. Besides its narrow 3.4 Å pore window and the one-dimensional (1D) sub-nanochannels, the Zn-P-dmbIm MOF powder can easily transform into liquid state (MOF liquid) upon heating under low temperature of 175 °C (Supplementary Fig. 2). The MOF liquid would transform into glass state (MOF Glass) after a rapid cooling process (Fig. 1c, the top panel). It worth noting that there are several differences between the Zn-P-dmbIm MOF powder and the MOF Glass. Even both of them all possess 1D channels, the MOF Glass exhibits much narrower pore windows of about 2.9 Å (Supplementary Fig. 3 and Supplementary Table 1). On the other hand, unlike crystalline Zn-P-dmbIm MOF powder with long-range ordered channels, MOF Glass possesses only short-range ordered channels, giving it an amorphous characteristic (Fig. 1c, the bottom panel, Supplementary Fig. 4). The MOF liquid demonstrates quite similar amorphous characteristic as that of the MOF Glass. These results inspired us to preparing MOF Glass infused high-voltage cathode using MOF liquid-infusion strategy. By melting the mixture of Zn-P-dmbIm MOF powder and cathode material, the low-viscosity and flowable MOF liquid can easily diffuse into the inner voids of the secondary cathode particles and constantly infuse into the grain boundaries between the primary cathode particles (Supplementary Fig. 5). Before a rapid cooling process, MOF liquid can completely wet the cathode from inside to outside (100% MOF coverage), and finally obtain cathode coated with rigid and thin MOF Glass (Fig. 1d, Supplementary Fig. 6). This unique coating effect cannot be achieved through typical strategies, such as simply mixing MOF particles with cathode materials. For example, when the MOF Glass is physically mixed with the NCM-811 cathode without further low-temperature treatment, it fails to successfully coating the NCM-811 (Supplementary Fig. 7). This highlights the importance of the MOF liquid-infusion

strategy with further low-temperature treatment for achieving even coverage. The seamless MOF Glass is expected to facilitate the particle-level Li-ions pre-desolvation (Fig. 1e, f, Supplementary Figs. 8-10). It was found that the thickness of the MOF Glass layer can be controlled by adjusting the amounts of MOF particles added. Obviously, NCM-811 materials with relatively lower MOF additions (0.25, 0.5 and 1 wt%) demonstrate a much thinner and less uniform MOF Glass coating (Supplementary Fig. 11, with parts of the NCM-811 particles left uncovered), while increasing the MOF additions (2, 5 and 10 wt%) leads to a thicker and much uniform MOF Glass layer (Fig. 1g, h, Supplementary Figs. 12-16). We find that a uniformly and thoroughly covered MOF Glass layer would effectively suppress direct contact between the electrolyte and cathode, thus significantly preventing particle cracks (Supplementary Fig. 17) and reducing transition metal dissolution and migration (defined as TM loss) (Supplementary Fig. 18). Notably, batteries utilizing NCM-811 cathodes coated with 5 wt% and 10 wt% MOF glass exhibited nearly the same TM loss as those with a 2 wt% MOF Glass coating. Additionally, NCM-811 cathodes with 2 wt%, 5 wt%, and 10 wt% MOF glass coatings all maintained good stability without significant cracking. These findings highlight the critical importance of a uniform and complete MOF Glass coating. However, increasing the thickness of the MOF Glass coating beyond 2 wt% does not lead to a further reduction in TM loss, likely because the cathodes are already effectively coated. We also find that Glass@NCM-811 cathode material with 2 wt% Glass coating demonstrates almost the same electrochemical performance as Glass@NCM-811 cathode material with 5 wt% and 10 wt% Glass coating (Supplementary Fig. 19). In general, a high mass loading of the MOF Glass coating on the NCM-811 cathode

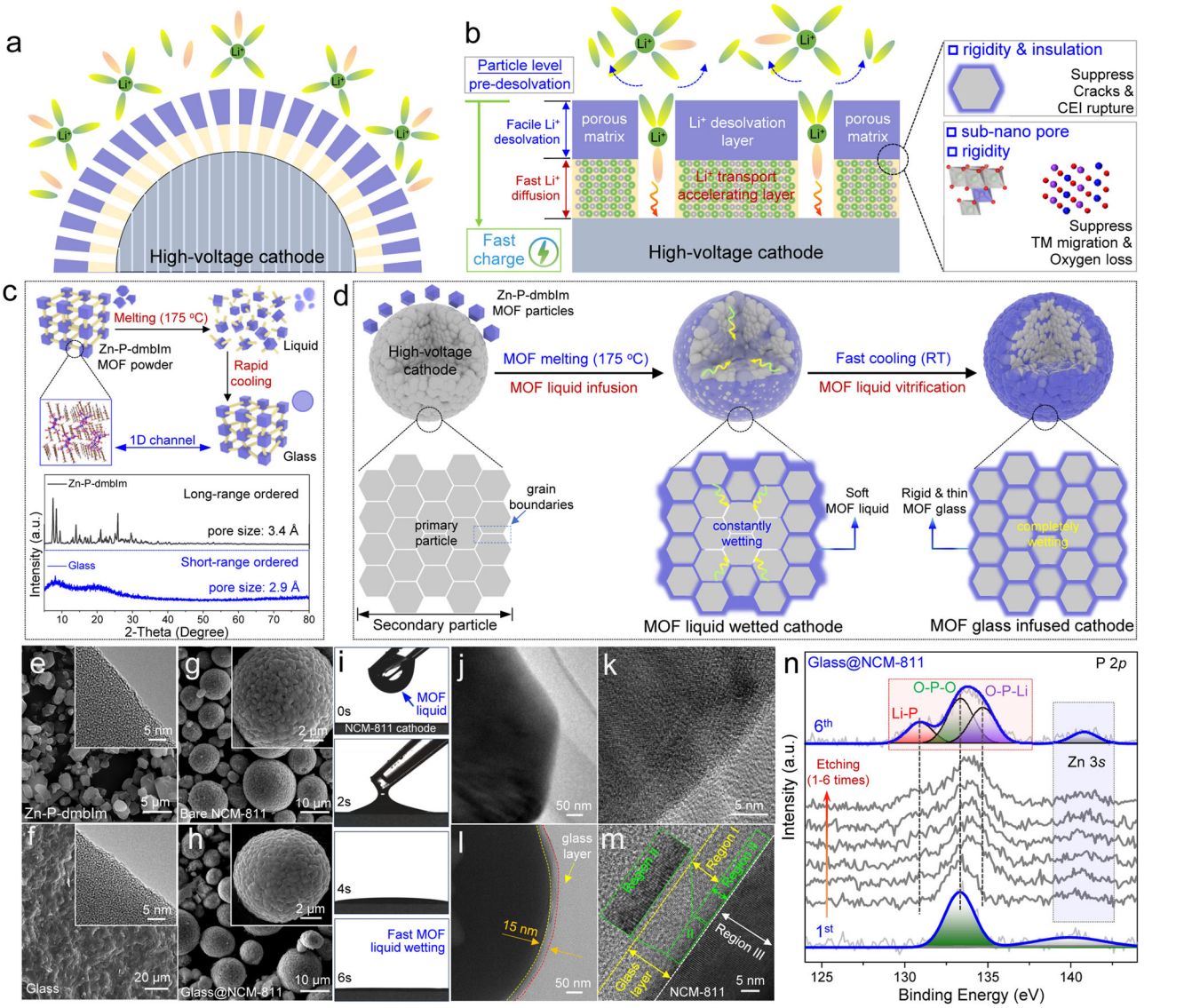

Fig. 1 | MOF liquid-infusion enabled MOF Glass infused high-voltage cathode to stabilize cathode stability and enhance fast Li-ion diffusion. a, **b** A double-layer coating is applied to the surface of the high-voltage cathode material, featuring an outer layer of non-conductive porous material with sub-nanometer channels which can promotes Li-ion pre-desolvation and an inner layer that facilitates rapid Li-ion conduction. **c** Schematic of the transformation of Zn-P-dmbIm MOF powder to MOF liquid and MOF Glass and the corresponding XRD patterns of Zn-P-dmbIm MOF powder and MOF Glass. **d** Schematic illustration of using MOF liquid-infusion strategy to prepare MOF Glass infused cathode, with the MOF liquid uniformly coated the surface of NCM secondary particle and infused into GBs between the NCM primary particles before MOF liquid vitrificated into MOF Glass. SEM and TEM images of (**e**) Zn-P-dmbIm MOF powder and (**f**) MOF Glass. SEM image of (**g**) bare NCM-811 and (**h**) Glass coated NCM-811 (Glass@NCM-811). **i** Contact angles of the MOF liquid on NCM-811 electrode. TEM images of (**j**, **k**) bare NCM-811 and (**l**, **m**) Glass@NCM-811. The TEM in (**m**) verified the uniform MOF Glass outer layer and the formation of inner layer. **n** In-depth etching XPS of the prepared Glass@NCM-811. XPS results confirmed that the inner layer was composed of components that accelerate Li-ion conduction.

increases fabrication costs and reduces the energy density of batteries utilizing the Glass@NCM-811 cathode material. Therefore, based on these afore-mentioned results, we think that a 2 wt% MOF Glass coating is the optimal thickness, and finally selected 2 wt% MOF Glass coated NCM-811 (shorted as Glass@NCM-811) as the as our main sample. In this article, for consistency, unless specified otherwise, Glass@NCM-811 refers to this configuration thereafter (Fig. 1h, Supplementary Fig. 20 and 21). The MOF Glass coating did not noticeably reduce the electrical conductivity of the cathode material, nor did it contribute additional capacity to the batteries with MOF Glass-coated cathodes. (Supplementary Fig. 22). More importantly, the MOF liquid, heated to 175 °C, can quickly wet the electrodes in just several seconds (Fig. 1i, Supplementary Fig. 23 and 24) benefits from the low viscosity of the MOF liquid[44]. This rapid wetting highlights the high efficiency of MOF liquid for quick infiltration and complete coating towards cathode primary/secondary particles. The corresponding TEM images and the corresponding Fourier-transform infrared spectroscopy (FTIR)/X-ray photoelectron spectroscopy (XPS) results verify the successful complete MOF Glass coating on NCM-811 (Fig. 1j–m, Supplementary Figs. 25-27). For the pristine bare NCM-811, only apparent layered structure can be clearly observed (Fig. 1j, k). For sharp contrast, a thin 15 nm Glass layer can be clearly found on the Glass@NCM-811 material (Fig. 1l). More importantly, we also find that a special inner region II within the MOF Glass layer (Fig. 1m, highlighted by the green rectangle line) can be clearly observed. Based on the high-resolution TEM (HR-TEM) image, the inner region II that directly attached with the NCM-811 demonstrates slightly narrower layered structure than that of the bare NCM-811. This unique structure is further verified by in-depth etching XPS measurements (Fig. 1n, Supplementary Fig. 28). In the P 2*p* XPS spectrum collected after the first etching, despite a weak peak related to Zn 3*s*, only a single peak corresponding to O-P-O (green curve, situated at about 133.3 eV) is observed[45]. This peak can be attributed to the P-O interactions within the MOF Glass (Fig. 1n). We also compare the XPS results collected after the first-time etching with that of the pristine MOF Glass and the surface of the Glass@NCM-811 cathode material without etching (Supplementary Fig. 29). The clear overlap of these three curves indicates that the outer layer (surface and after one-time etching) of the Glass@NCM-811 still belongs to the electrically non-conductive MOF Glass. As the etching progresses, two new peaks appear at about 130.9 and 134.7 eV, which can be assigned to Li-P and O-P-Li interactions, respectively (Fig. 1n). It has been reported that Li-P and O-P-Li components can accelerate Li-ion diffusion and enhance the rate performance of batteries[46]. Therefore, based on these results, we conclude that this MOF liquid-infusion strategy successfully constructs a unique double-layered Glass structure on the surface of the NCM-811, with the outer-layer consisting of electrically non-conductive porous MOF Glass with 2.9 Å pore windows and the inner-layer comprising Li-ion conducting components. It is believed that chemical reactions occurred during the MOF liquid phase at 175 °C and the MOF glass formation process (rapid cooling to 25 °C), leading to the formation of a Li-ion conductive layer containing Li-P and Li-P-O components.

Fast Li-ion desolvation and diffusion of the Glass@NCM-811 cathode

To study the functions of this unique MOF Glass coating, further characterizations are conducted. In the XRD pattern, the intensity ratio between (003) and (104) peaks ($I_{(003)}/I_{(104)}$) of the Glass@NCM-811 is nearly the same as that of the bare NCM-811, which indicates the Glass coating does not severally damage the layered structure of NCM-811 (Fig. 2a)[47]. Both the bare NCM-811 and Glass@NCM-811 are coupled with metallic Li to evaluate their rate performances. Compared with the cell based on bare NCM-811 which demonstrates poor rate performance, the Li||Glass@NCM-811 battery exhibits much good rate performance from 0.1 C to as high as 5 C current rates. The biggest difference comes from the capacity obtained under 5 C, in where the Li||Glass@NCM-811 battery delivers about 165 mAh g^{-1} capacity, while the bare NCM-811//Li battery sustains only 80 mAh g^{-1} (Fig. 2b). This indicates that the MOF Glass constructs on NCM-811 surface can remarkably enhance the Li-ion transporting rate during battery discharge/charge processes. The state of charge (SoC) vs. time curves of bare Li||NCM-811 and Li||Glass@NCM-811 cells are also tested under constant current-constant voltage (CC-CV) mode (see Experimental Section for detail). As shown in Fig. 2c, the Li||Glass@NCM-811 cell reaches 100% state of charge (SoC) in just 1080 seconds, much faster than the bare Li||NCM-811 cell, which takes 1400 seconds. Additionally, under CC mode, the Li||Glass@NCM-811 cell achieves a much higher SoC of 75%, compared to only 41% for the bare Li||NCM-811 cell. This is benefits from the remarkably low interfacial resistance of Li||Glass@NCM-811 cell[38,46]. Then, galvanostatic intermittent titration technique (GITT) measurements of two cells are measured after 100 cycles (same cells in Fig. 2b after rate performance test). Obviously, the bare Li||NCM-811 cell exhibits significantly higher battery polarization, with an average voltage loss approximately 3.5 times higher than that of the Li||Glass@NCM-811 cell (0.14 V vs. 0.04 V, Fig. 2d). The corresponding Li^+ diffusion coefficient of the battery based on Glass@NCM-811 is one order of magnitude higher than that of the cell assembled with pristine NCM-811 cathode (Supplementary Fig. 30), demonstrates that the MOF Glass coating significantly enhances lithium diffusion kinetics. These results collectively verify the crucial role of the MOF Glass coating, particularly the inner-layer of the Glass, in promoting fast Li-ion diffusion in the NCM-811 cathode. The outer-layer of MOF Glass is also under further investigation by FTIR and Raman spectroscopy. In order to facilitate our data collection, we increase the thickness of the MOF Glass layer (see Experimental Section for detail). Then, by etching away the surface MOF Glass layer (about 2 nm, see Experimental Section for detail), we detect the electrolyte information inside the MOF Glass. Compared with the FTIR result of typical electrolyte (1 M $LiPF_6$-EC/DMC, the bottom panel in Fig. 2e), electrolyte signals detect from inside the surface MOF Glass demonstrate much stronger Li^+-solvent interactions (Li-EC and Li-DMC, the top panel in Fig. 2e). This indicates that the electrolyte forms an aggregative configuration inside the MOF Glass[41], highlighting the crucial role of MOF Glass in facilitating Li-ion pre-desolvation and accelerating Li-ion migration before reaching the NCM-811 cathode surface[46]. Raman data of electrolyte inside MOF Glass layer and $LiPF_6$-EC/DMC electrolytes with different concentrations consists well with the FTIR result (Supplementary Fig. 31), which further verifies the effectiveness of MOF Glass in promoting pre-desolvation of Li-ions. Considering the average pore window of the MOF Glass and the sizes of solvent molecules and PF_6^-, we propose that the pre-desolvated Li-ions confined inside the MOF Glass channel maintain configuration as schematically illustrated in in Supplementary Fig. 32.

EIS measurement is used to calculate the activation energy during Li-ion (pre) desolvation and its migration/transport across the cathode electrolyte interphase (CEI) (Supplementary Figs. 33 and 34). To simplify the calculation process, we combine the activation energies from both processes for a unified calculation. Clearly, the activation energy (E_a) of Li||Glass@NCM-811 cell is 45.7 kJ mol^{-1}, which is much lower than 104.3 kJ mol^{-1} of bare Li||NCM-811 cell (Fig. 2f). The facile Li-ion pre-desolvation and fast Li-ion transport is further verified by data shown in Fig. 2g. Compared with the energy barrier (42.6 kJ mol^{-1}) of Li-ion desolvation within bare NCM-811, the much lower energy barrier (19.3 kJ mol^{-1}) during Li-ions pre-desolvation of the Glass@NCM-811 further verifies the facile Li-ion pre-desolvation inside the 2.9 Å pore windows of MOF Glass outer-layer. Additionally, the significantly lower energy barrier for Li-ion transport in Glass@NCM-811 (26.4 kJ mol^{-1} compared to 61.7 kJ mol^{-1} for bare NCM-811) indicates much faster Li-ion diffusion through the dual-layer structure of Glass on NCM-811 surface. We attribute the significantly reduced pre-desolvation and Li-ion transport activation energy of Li||Glass@NCM-811 to the narrow

https://doi.org/10.1038/s41467-025-58639-z

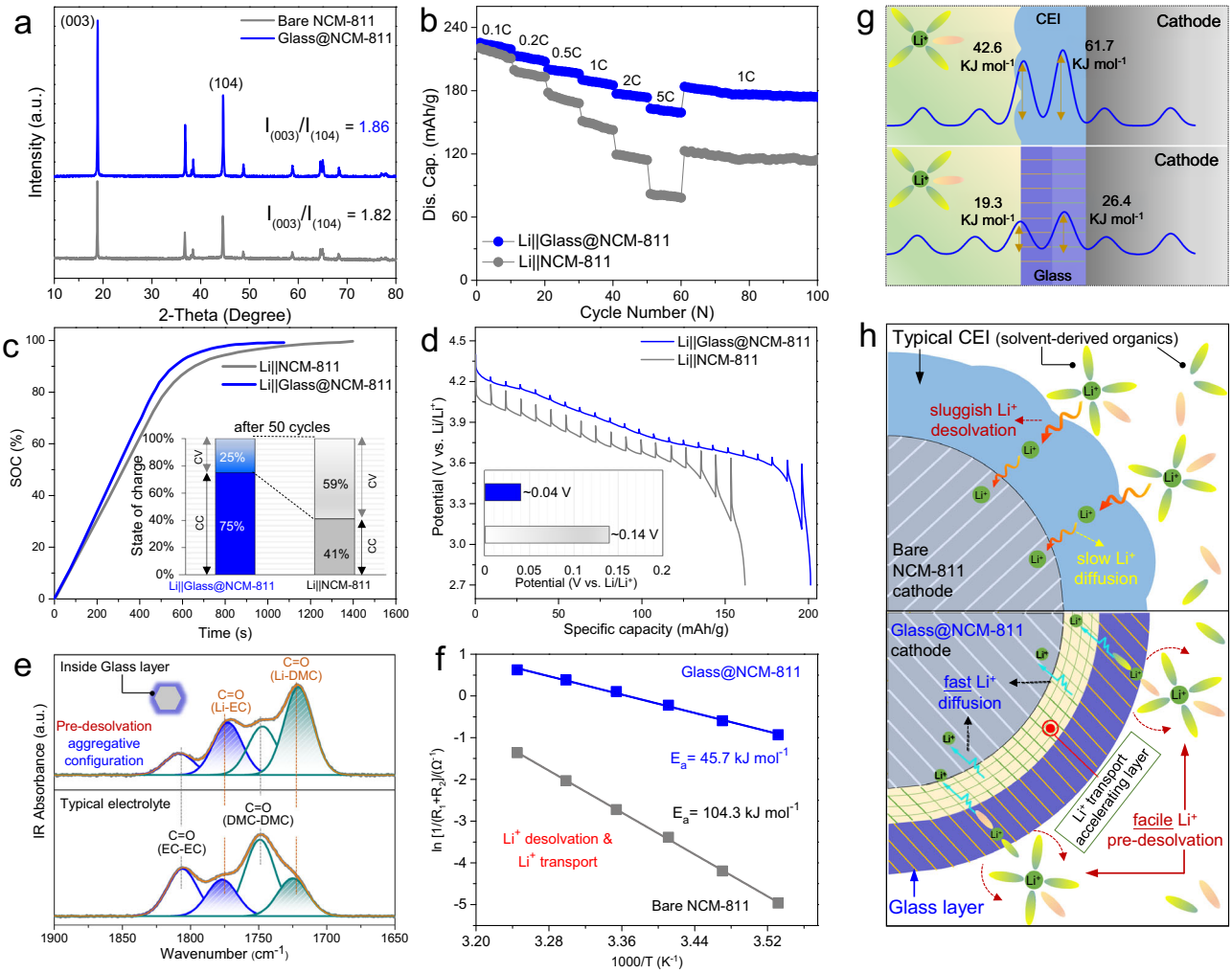

Fig. 2 | The MOF Glass coating positively stabilizes the NCM cathode and enhances Li-ion desolvation and transport. a XRD patterns of bare NCM-811 and Glass@NCM-811 cathodes. **b** Rate performances of batteries based on bare NCM-811 and Glass@NCM-811 cathodes (defined 1 C = 220 mA/g). **c** The state of charge (SoC) vs. time curves of Li||NCM-811 and Li||Glass@NCM-811 cells. This indicated the much faster Li-ion desolvation and transport of Li||Glass@NCM-811 cell due to the much lower interfacial resistance. **d** Discharge curves of the GITT measurements conducted after the 100th cycle (same cells used in Fig. 2b). Inset: average voltage loss and its standard deviation over different GITT steps. **e** FTIR spectra of typical electrolyte ($LiPF_6$-EC/DMC, the bottom panel) and electrolyte formed inside the Glass layer (the top panel). The aggregative electrolyte inside the Glass layer suggested the successfully pre-desolvation enabled by the sub-nanochannels of the Glass layer. **f** Comparison of activation energies during Li-ion desolvation and its migration across the cathode electrolyte interphase (CEI) for Li||NCM-811 and Li||Glass@NCM-811 cells. **g** Comparison of the kinetics of desolvation/pre-desolvation and Li-ion transport through the cathode electrolyte interphase (CEI) in Li||NCM-811 cell (the top panel) and Li||Glass@NCM-811 cell (the bottom panel). **h** Schematic illustration of solvated Li-ions penetrating through the typical CEI formed on cycled bare NCM-811 cathode (top panel) and Glass layer on cycled Glass@NCM-811 cathode (bottom panel).

2.9 Å pore windows of the MOF Glass outer layer, which facilitate facile Li-ion pre-desolvation and create an aggregated electrolyte with a low-solvent-coordination solvation structure[46]. Additionally, the inner-layer, containing Li-ion transport-accelerating components (Li-P and O-P-Li), promotes fast Li-ion transport. Based on those obtained results, we propose how Li-ions passing through the typical CEI (mainly solvent-derived organics) on bare NCM-811 and Glass layer of Glass@NCM-811 cathode (Fig. 2h).

Glass@NCM-811 cathode suppresses cathode cracks, CEI rapture, cation mixing and side-reactions

The cycled bare NCM-811 and Glass@NCM-811 cathodes underwent further characterization to study the additional positive effects of the MOF Glass coating. After cycling, the bare NCM-811 cathodes show extensive side-reaction byproducts covering their surface (Fig. 3a, Supplementary Fig. 35). In sharp contrast, the cycled Glass@NCM-811 cathodes exhibit much smoother surfaces without various byproducts accumulation (Fig. 3c, Supplementary Fig. 36), indicating significantly suppressed electrolyte decomposition. Elemental mapping results corroborate the SEM images of the two cycled cathodes (Supplementary Figs. 37 and 38). Furthermore, apparent cracks are observed inside the cycled bare NCM-811 cathodes (Fig. 3b, Supplementary Figs. 39 and 40), whereas no obvious cracks were found inside the cycled Glass@NCM-811 cathodes (Fig. 3d, Supplementary Figs. 41 and 42). The TEM elemental mapping of the two cycled cathodes shows substantial differences, with disorganized and uneven distributions of elements, especially P and F, in the cycled bare NCM-811 cathodes, indicating severe byproduct accumulation from electrolyte solvent decompositions (Supplementary Fig. 43). In sharp contrast, the cycled Glass@NCM-811 cathode demonstrates uniform distributions of elements (Fig. 3e–j). The Glass coating remains intact even after various discharge/charge processes, further verifying the MOF Glass's role in protecting the NCM-811 cathode. Notably, the F element mapping is slightly smaller than the cycled Glass@NCM-811

https://doi.org/10.1038/s41467-025-58639-z

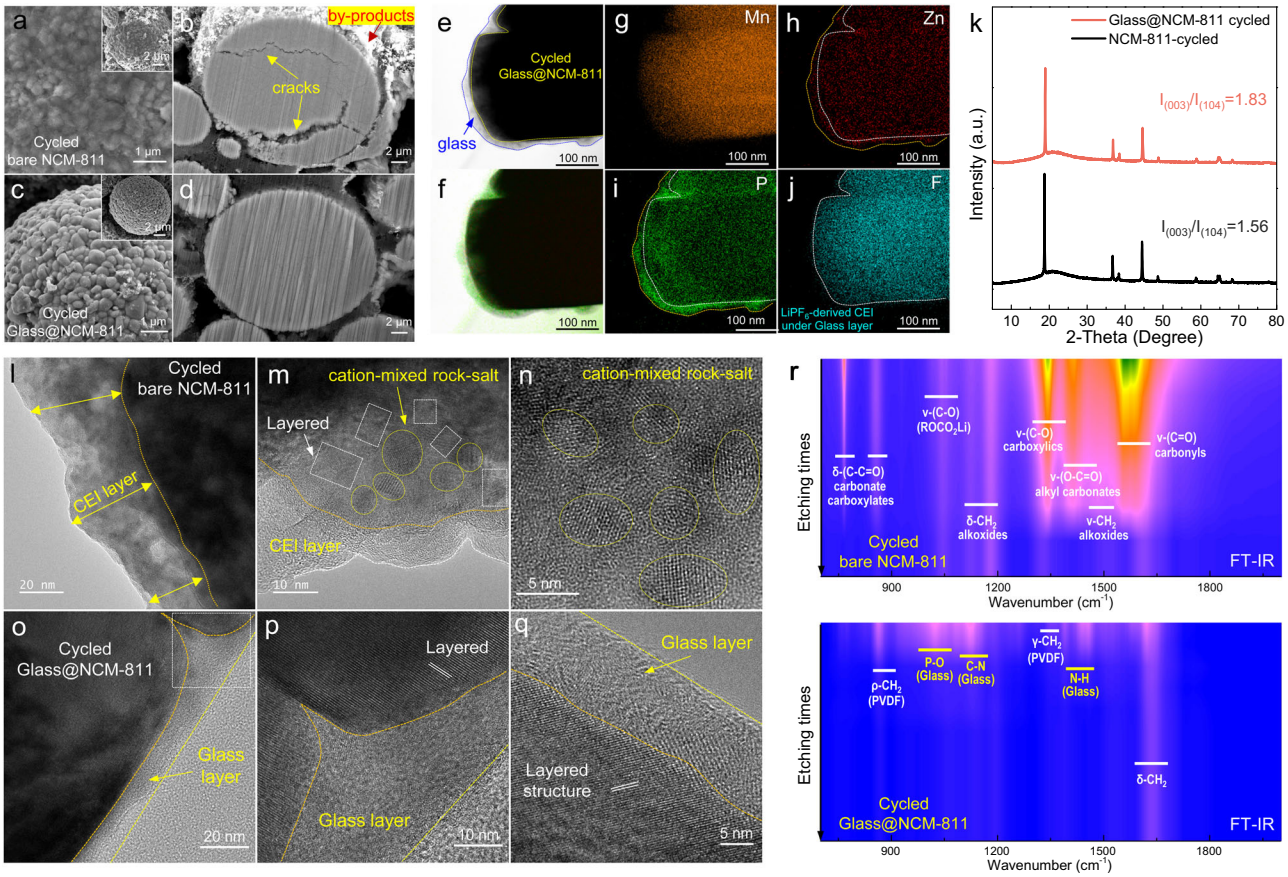

Fig. 3 | The MOF Glass infusion strategy stabilizes NCM-811 cathode by effectively suppressing cathode cracks, CEI rapture, cation mixing and side-reactions. a SEM image and **b** cross-sectional SEM image of the cycled NCM-811 after 200 cycles. **c** SEM image and **d** cross-sectional SEM image of the cycled Glass@NCM-811 after 400 cycles. **e**–**j** TEM image and the corresponding elemental mapping images of the cycled Glass@NCM-811. **k** XRD of cycled Glass@NCM-811 and cycled bare NCM-811. **l**–**n** High-resolution transmission electron microscopy (HR-TEM) images of the cycled bare NCM-811. **o**–**q** HR-TEM images of the cycled Glass@NCM-811. **r** In-depth etching FTIR of the cycled bare NCM-811 cathode (the top panel) and the cycled Glass@NCM-811 (the bottom panel).

cathode, and its shape corresponds well with the NCM-811 under the MOF Glass coating (Fig. 3j). Since the only source of F is the $LiPF_6$ salt, we attribute this to the decomposition of the PF_6 anion under the electrically non-conductive MOF Glass layer, further confirming the pre-desolvation of Li-ions through the MOF Glass sub-nanochannels. Additionally, the cycled Glass@NCM-811 demonstrates much higher $I_{(003)}/I_{(104)}$ value than the cycled NCM-811 cathode, which suggest it does not experience serious structural degradation even after multiple electrochemical cycles (Fig. 3k). The differential capacity (dQ/dV) curves of two cells based on pristine NCM-811 and Glass@NCM-811 cathode are also recorded (Supplementary Fig. 44). For bare NCM-811 based cell, the H2/H3 (second hexagonal to third hexagonal) gradually disappear and the other redox peaks (hexagonal to monoclinic, H1/M; monoclinic to second hexagonal, M/H2) diminish, which was closely related to cracks apparition[48]. This indicates that mechanical stress generated cracks in the cathode along the grain boundaries, and the layered structure collapse over 100 cycles. Compared with that of the battery based on bare NCM-811, the cell assembled with Glass@NCM-811 cathode exhibits a reversible redox peak for the H2/H3 transition even after 100 cycles. This indicates the MOF Glass helping in protecting the cathode from structural volume changes, which again underscoring the significant role of MOF Glass in stabilizing the NCM-811 cathode. Most cathode materials are highly susceptible to degradation when exposed to water, with even minimal contact severely impacting their electrochemical performance. Remarkably, the Glass@NCM-811 cathode exhibits good water resistance, maintaining its performance even under such conditions (Supplementary Fig. 45). Specifically, the battery assembled with water-immersed Glass@NCM-811 cathode (after 7 days of immersion) exhibits almost the same electrochemical performance as a battery with a fresh Glass@NCM-811 cathode (Supplementary Fig. 46).

TEM studies of the two cycled cathodes reveal further insights. For the cycled bare NCM-811 cathode, thick and uneven cathode electrolyte interphase (CEI) layers, varying from 30 to 60 nm and in some cases reaching up to 80 nm, are distinctly observed (yellow arrows highlighted in Fig. 3l and Supplementary Figs. 47, 48). More importantly, various cation-mixed rock-salt phases are observed after cycling (Fig. 3m, n and Supplementary Fig. 47e, 47f, highlighted with yellow circles), indicating serious cation mixing originating from surface oxygen loss followed by surface cation densification. In stark contrast, the layered structure of the cycled Glass@NCM-811 and the Glass layer is well preserved, with no obvious cation-mixed rock-salt phases detected (Fig. 3o–q and Supplementary Figs. 49, 50). This further confirms the MOF Glass coating's critical role in preventing cation mixing and stabilizing the cathode. In-depth etching FTIR measurement is used to investigate the surface information of cycled two cathodes. For the cycled bare NCM-811 cathode (Fig. 3r, the top panel), tremendous EC electrolyte solvent decomposition induced byproducts (carboxylics (C-O), alkyl carbonates ($ROCO_2Li$) and carbonyls (C = O)) can be clearly found during the whole etching process. Interestingly, during the initial etching of the cycled Glass@NCM-811 cathode, only faint peaks corresponding to the PVDF binder and MOF Glass layer components (P-O, C-N, and N-H) are detected. Notably, there are almost no peaks related to the decomposition products of

https://doi.org/10.1038/s41467-025-58639-z

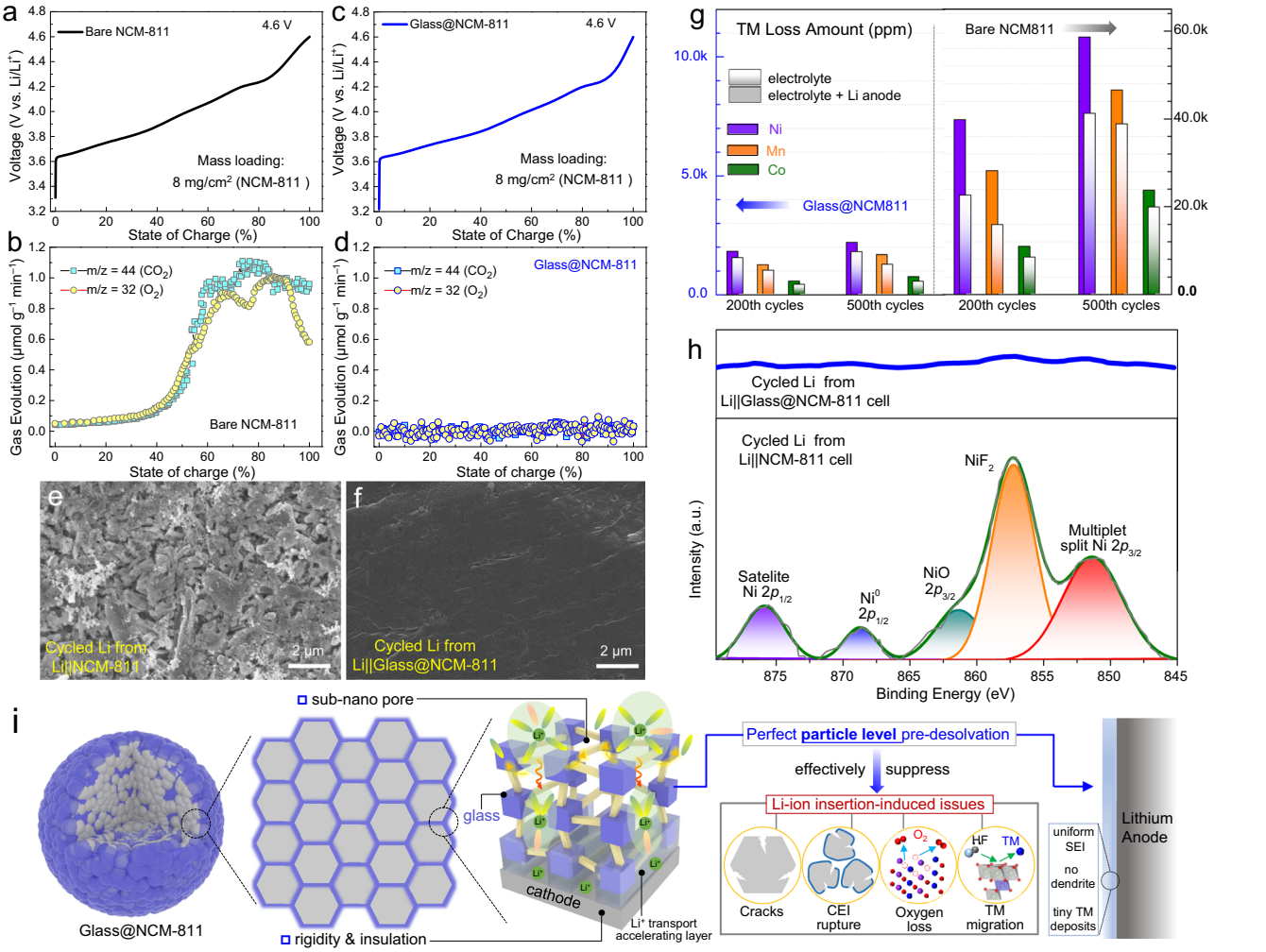

Fig. 4 | The MOF Glass infusion strategy stabilizes NCM-811 cathode by significantly eliminating oxygen loss, transition metal dissolution and migration. **a**, **b** Charge curve of bare Li||NCM-811 cell cycled for in-situ Differential Electrochemical Mass Spectrometry (in-situ DEMS) test and the corresponding DEMS data. **c**, **d** Charge curve of Li||Glass@NCM-811 cell cycled for in-situ DEMS test and the corresponding DEMS data. SEM of the cycled Li anode harvested from the cycled (**e**) bare Li||NCM-811 cell and (**f**) Li||Glass@NCM-811 cell after 400 cycles. **g** Dissolved transition metals inside the cycled electrolyte and on the cycled Li anode from Li||Glass@NCM-811 (the left panel) and Li||NCM-811 cell (the right panel) by ICP-OES after different cycles. **h** Ni XPS results collected on the cycled Li anode from Li||Glass@NCM-811 (the top panel) and Li||NCM-811 cell (the bottom panel). **i** Schematic illustration of the MOF Glass infusion strategy shows stabilization of the NCM-811 cathode by suppressing issues induced by electrolyte penetration and solvated Li-ion/solvent co-insertion, including cathode particle cracks, CEI rupture, oxygen loss, and transition metal migration. By implementing the perfect particle-level pre-desolvation method, both the stability of cathode and Li anode can be greatly enhanced.

the EC solvent (Fig. 3r, the bottom panel). Those results together verify the significant role of non-conductive MOF Glass coating in suppressed cathode cracks, CEI growth, cation mixing and side-reactions.

Glass@NCM-811 cathode significantly eliminates gases generation, transition metal dissolution/migration

In-situ differential electrochemical mass spectrometry (In-situ DEMS) measurements are employed to investigate gas generation in cells based on bare NCM-811 and Glass@NCM-811 cathodes. The bare Li|| NCM-811 battery produces significant amounts of carbon dioxide and oxygen (CO_2/O_2) (Fig. 4a, b and Supplementary Fig. 51a, 51b), whereas the Li||Glass@NCM-811 battery generates only negligible amounts of gas during the electrochemical cycling process (Fig. 4c, d). The corresponding ^{1}H Nuclear magnetic resonance (NMR) analysis results of cycled electrolytes collected from the two batteries suggest that the Li||Glass@NCM-811 cell exhibits greatly suppressed electrolyte decomposition than its counterpart (Supplementary Fig. 51c). These results suggest that the MOF liquid infusion coating strategy effectively lowers surface and grain boundary oxygen activity and suppresses electrolyte solvent oxidation. The complete MOF Glass coverage effectively prevents electrolyte penetration into the interior of the NCM-811 cathode, and the aggregative electrolyte formation inside the MOF Glass sub-nanochannels during Li-ion pre-desolvation together contributing to the suppression of electrolyte oxidation and gas generation. We also observe distinct differences in the morphologies of the cycled Li anodes collected from the two batteries. The cycled Li anode from the bare Li||NCM-811cell exhibits a porous layer consisting of mossy Li and unevenly distributed byproducts (Fig. 4e), whereas the Li anode from the Li||Glass@NCM-811 cell maintains a smooth surface without any dendrites and byproducts (Fig. 4f). This smooth, dendrite-free Li anode is likely due to the greatly suppressed transition metal dissolution/migration. Generally, the deposited TM would degrade the performance of the Li anode. To further support this, we assembled Li//Li symmetric cells using electrolytes with/without 400 ppm $Ni(TFSI)_2$ salt (see Experimental Section for detail). As shown in Supplementary Fig. 52, the Li//Li symmetric cell with 400

https://doi.org/10.1038/s41467-025-58639-z

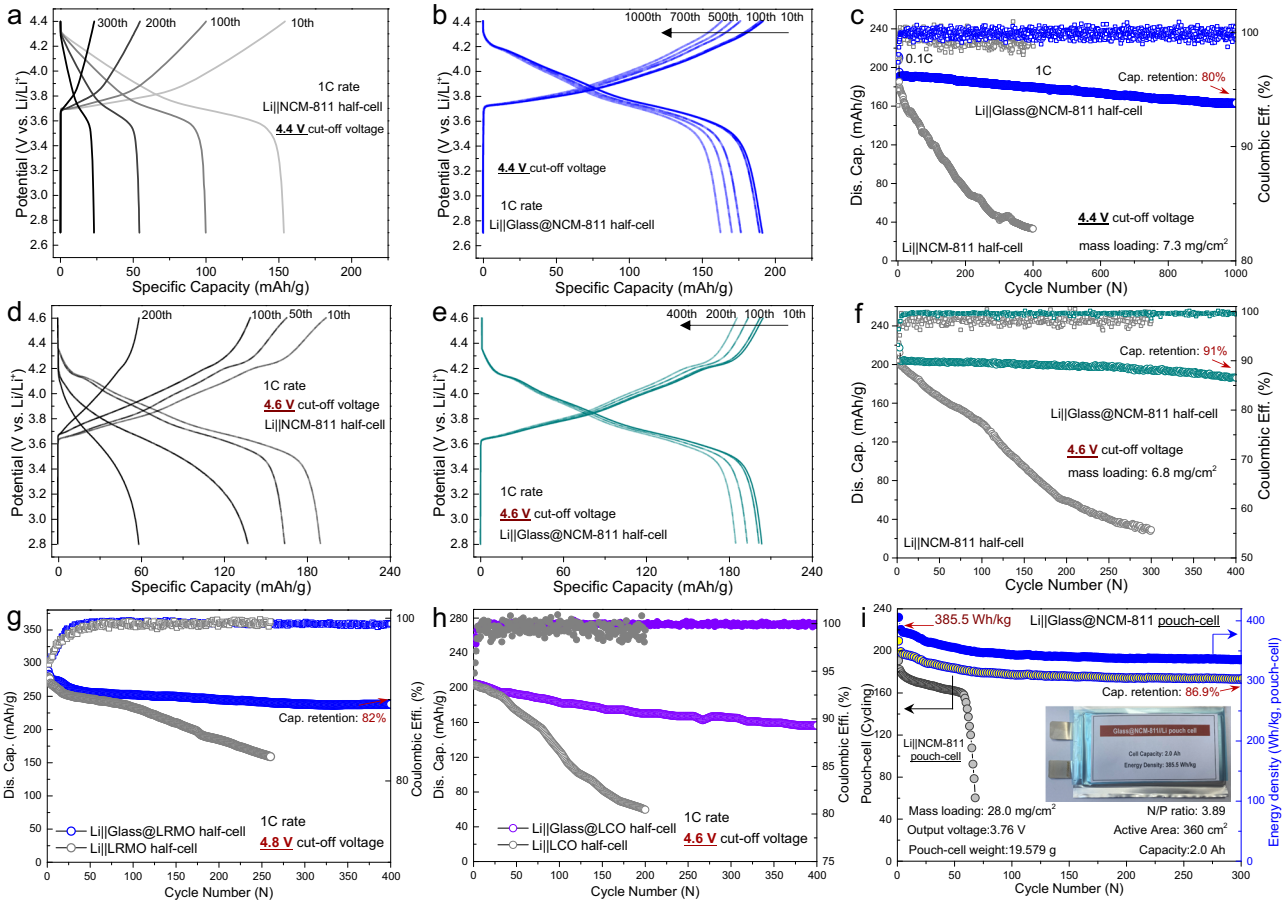

Fig. 5 | Superior electrochemical performance of Li||Glass@NCM-811 battery over bare Li||NCM-811 battery. Cycling performances and the corresponding discharge/charge curves of Li||Glass@NCM-811 cell (blue/green curves) and Li||NCM-811 cell (light grey curves) cycled under the range of (**a**-**c**) 2.7–4.4 V and (**d**–**f**) 2.8–4.6 V (defined 1 C = 220 mA/g for NCM-811 based batteries). **g** Cycling performance of Li||Glass@LRMO cell and Li||LRMO cell under 4.8 V cut-off voltage (defined 1 C = 280 mA/g for LRMO based batteries). **h** Cycling performance of Li||Glass@LCO cell and Li||LCO cell under 4.6 V cut-off voltage (defined 1 C = 220 mA/g for LCO based batteries). **i** 385 Wh kg^{-1}-level Li||Glass@NCM-811 pouch-cell and cycling performance of pouch-cell based on bare Li||NCM-811. Inset: the digital photo of the Li||Glass@NCM-811 pouch-cell.

ppm $Ni(TFSI)_2$ salt added electrolyte short-circuited much faster than the cell without $Ni(TFSI)_2$ salt addition, indicating that the deposited Ni-induced morphological instability would degrade the performance of the lithium-metal anode. Corresponding ICP results of bare Li||NCM-811 and Li||Glass@NCM-811 batteries are also recorded. As shown in Fig. 4g, the bare Li||NCM-811 battery (right panel) experiences more than 20 times higher TM loss than its Li||Glass@NCM-811 counterpart (left panel) after 200 and 500 cycles, respectively. Obviously, the Li anode collected from the bare Li||NCM-811 cell showed significantly higher TM deposits than the Li anode from the Li||Glass@NCM-811 battery (Fig. 4g, the gap between fully-dyed and semi-dyed rectangles). Additionally, we also evaluate the electrochemical performance and transition metal (TM) loss in a bare Li||NCM-811 battery with MOF Glass directly coated on the NCM-811 electrode, termed Glass-NCM-811 (Supplementary Fig. 53a-c). The Li||Glass-NCM-811 cell demonstrates significantly improved cycling stability and considerably reduced TM loss compared to the bare Li||NCM-811 battery (Supplementary Fig. 53d-f). Notably, the cycled Glass-NCM-811 cathode also exhibits much thinner and more uniform CEI layers across various cycles (Supplementary Fig. 54) compared to the bare NCM-811 cathodes (Fig. 3l–n, Supplementary Fig. 48), underscoring the benefits of electrode-level Glass coating. Nevertheless, despite these advantages, the TM loss of Li||Glass-NCM-811 cell is slightly higher and the electrochemical stability lower than that of the Glass@NCM-811//Li battery, emphasizing the superior performance provided by particle-level Glass coating (Supplementary Fig. 53d-f). The XPS of Li anodes from two batteries also demonstrate the same results. By using XPS measurement, we find the SEI of Li anode from Li||Glass@NCM-811 battery exhibits much weaker Ni element signals than the Li anode pairs with bare Li||NCM-811 battery (Fig. 4h). Based on those results we have obtained in Figs. 2–4, we conclude that the MOF liquid infusion strategy effectively suppresses cathode particle cracks, CEI rupture, gas generation, and TM loss. By implementing this perfect particle-level pre-desolvation method, both the stability of cathode and Li anode can be greatly enhanced (Fig. 4i).

Enhanced cycling stability and energy density

The cycling stability and energy density are evaluated in both coin-cell and pouch-cell configurations by pairing MOF Glass-coated high-voltage cathodes with Li anodes. When cycles at a 1 C rate under a 4.4 V cut-off charge voltage, the bare Li||NCM-811 coin-cell demonstrates rapid capacity decay (Fig. 5a, c) after only 400 cycles. In sharp contrast, the Li||Glass@NCM-811 coin-cell exhibits remarkably enhanced cycling performance, retaining 80% of its capacity (calculated from the fourth cycle) after a long 1000 cycles (Fig. 5b, c). This trend is even more apparent when the cells are cycled under an elevated 4.6 V cut-off charge voltage. The bare Li||NCM-811 coin-cell fails quickly after only 300 cycles, while the Li||Glass@NCM-811 coin-cell delivers a high specific capacity of 180 mAh g^{-1} after 400 cycles (Fig. 5d–f). It worth noting that the MOF Glass layer within Glass@NCM-811 remains intact

without any apparent morphological changes, even after cycling at a high voltage of 4.6 V (Supplementary Fig. 55a). The XPS data of the cycled Glass@NCM-811 closely matches that of the uncycled sample, further indicating the good structural stability of the MOF Glass (Supplementary Fig. 55b, 55c). Two other typical high-voltage cathodes, Li-rich manganese (LRMO) and $LiCoO_2$ (LCO), are also coated with MOF Glass and paired with Li anodes to evaluate their cycling stability. Similarly, the Glass@LRMO and Glass@LCO coin-cells demonstrated superior performance compared to cells without MOF Glass coating. It is widely acknowledged that LRMO cathodes tend to suffer from severe voltage attenuation, rapid capacity decay, and poor cycling stability during electrochemical cycling, especially under high cut-off voltage. This is evidenced by the poor cycling performance of the Li||LRMO coin-cell under a high 4.8 V cut-off voltage, which maintains a capacity of 158.3 mAh g^{-1} after 260 cycles (only 56% capacity retention, calculated from the 3rd cycle). Remarkably, the Li||Glass@LRMO coin-cell demonstrates good cycling performance (Fig. 5g), retaining a high capacity of 237.8 mAh g^{-1} after 400 cycles (82% capacity retention, calculated from the 3rd cycle). The same trend was observed for the Li||Glass@LCO coin-cell, which also showed much more stable cycling than the Li|| LCO coin-cell (Fig. 5h). The corresponding first galvanostatic curves of different coin cells demonstrated in Fig. 5a-h can also be found as shown in Supplementary Fig. 56. These results further underscore the universality and importance of using MOF Glass coating to improve the stability of high-voltage cathode materials.

Inspired by these promising results, a 2.0 Ah-level pouch-cell consisting of Glass@NCM-811 and a Li anode was fabricated (Fig. 5i, inset). The Li||Glass@NCM-811 pouch-cell exhibits improved cycling stability, retaining 86.9% of its capacity (calculated from the 2nd cycle) after 300 cycles (Supplementary Fig. 57), compared to 37.6% capacity retention (calculated from the 2nd cycle) after 58 cycles for the bare Li|| NCM-811 pouch-cell (grey curve in Fig. 5i, Supplementary Fig. 58). Based on the pouch-cell parameters (Supplementary Table 2), the output energy density of the Li||Glass@NCM-811 pouch-cell is calculated to be as high as 385.5 Wh kg^{-1} (calculates from the 2nd cycle, 19.579 g for the whole pouch-cell). These electrochemical performances achieved with this MOF liquid infusion strategy rank among the highest compared to other state-of-the-art coating strategies (Supplementary Tables 3-6). Noting that all these performances are achieved on a laboratory scale, we believe that the pouch-cell energy density and cycling stability can be further improved to over 400 Wh kg^{-1} by optimizing the pouch-cell parameters, especially electrolyte modification. In addition, the MOF liquid infusion strategy used to create MOF glass-coated cathodes in this work is fundamentally different from other studies employing MOF glasses. And the key novelty of our work lies in its unique structure and specialized functions (Supplementary Fig. 59, Supplementary Table 7)[49–52]. The MOF liquid infusion strategy for preparing highly stable high-voltage cathodes offers promising prospects for practical industrial battery production, thanks to its good electrochemical performance and its simple, cost-effective, and time-efficient synthesis process.

In summary, we introduce a straightforward and efficient metal-organic framework (MOF, Zn-P-dmbIm) liquid-infusion strategy that fully infuses MOF liquid into the grain boundaries of high-voltage cathodes like NCM-811, LRMO, and LCO, achieving complete MOF Glass coverage (e.g., Glass@NCM-811). The surface electrically non-conductive MOF Glass layer with 2.9 Å pore windows facilitating Li-ion pre-desolvation and enabling highly aggregative electrolyte formation inside the Glass channels, suppressing solvated Li-ion co-insertion and solvent decomposition. While the inner Glass layer attaches with cathode composes of Li-ion conducting components and enhancing fast Li-ion diffusion. This MOF Glass coating prevents cathode particle cracks, CEI rupture, gas generation, and transition metal migration, while promoting rapid Li-ion transport. Consequently, Li||Glass@NCM-811 cells exhibit superior electrochemical performance, with remarkable rate capability and cycling stability, even at high charge rates (5 C) and elevated voltages (4.6 V). Similarly, Li||Glass@LRMO and Li||Glass@LCO batteries demonstrate good cycling stability over 400 cycles at 4.8 V and 4.6 V, respectively. The practical viability of this strategy is underscored by successfully achieving a 385 Wh kg^{-1}-level pouch cell using Glass@NCM-811.

Methods

All the chemicals employed in this synthesis section were purchased without additional exception.

Preparation of Zn-P-dmbIm MOF powder

Typically, $Zn(OAc)_2 \cdot 2H_2O$ (439 mg, 2 mmol, Sigma-Aldrich), 5,6-dimethylbenzimidazole (584.8 mg, 4 mmol, Sigma-Aldrich), and phosphoric acid (420 µL, 6 mmol, Sigma-Aldrich) were placed in a mortar and manually ground for 15 minutes. The powder was washed with dichloromethane three times and dried at 70 °C for 10 h. Then, the Zn-P-dmbIm MOF powder was obtained.

Synthesis of MOF glass

The as-prepared Zn-P-dmbIm MOF powder was heated under 175 °C under vacuum for 30 minutes before fast cooling to room temperature (25 °C). During this low temperature heating process, Zn-P-dmbIm MOF powder transformed into MOF liquid and went rapid vitrification to form MOF Glass (Zn-P-dmbIm Glass). The as-prepared MOF Glass was then used for further physical/chemical measurements.

Synthesis of MOF glass film

MOF Glass film was also prepared for diffusion test to verify its crack-free property. Typically, the as-prepared Zn-P-dmbIm MOF powder was mechanically pressed into pellets with diameter of 15 mm under 2 MPa for 60 seconds, and the obtained pellets were heated under 175 °C under vacuum for 30 minutes to melt the Zn-P-dmbIm MOF powder into MOF liquid and then MOF Glass. The self-standing film was obtained after rapid cooling to room temperature. The prepared MOF Glass film was then sandwiched between a home-made V-type device, with one side filled by LiTFSI-G_3 (lithium bis(trifluoromethanesulfonyl)imide (LiTFSI) solvated by triethylene glycol dimethyl ether(G3), Sigma-Aldrich, 2 mL) and the other side injected with LiTFSI-Pyr_{13}TFSI (Aladdin Scientific Corp., 2 mL). Certain trace amount of electrolyte (40 µL per time) can be taken out for IR observation after aging to verify the crack-free property of the MOF Glass with sub-nano pore windows of 2.9 Å.

Synthesis of MOF glass coated high-voltage cathodes

The $LiNi_{0.8}Co_{0.1}Mn_{0.1}O_2$ (NCM-811) cathode was purchased from Tianjin Lishen Battery Joint-Stock Co., LTD. Li-rich manganese oxides (LRMO) and $LiCoO_2$ (LCO) cathode was purchased from Dodochem Co,. Ltd. To prepare MOF Glass coated cathodes, the as-prepared Zn-P-dmbIm MOF powder was mixed with cathode materials (including NCM-811, LRMO, LCO etc.). And the weight ratio between cathodes and Zn-P-dmbIm MOF powder were varies from 2 wt% to 5 wt%, and 10 wt% in a mortal and manually ground for 10 minutes. The mixtures were then heated under 175 °C under vacuum for 30 minutes before fast cooling to room temperature (25 °C). Finally, the MOF Glass coated cathode materials were successfully obtained, and defined as Glass@NCM-811, Glass@LRMO, and Glass@LCO, respectively. Based on the results obtained, we found the 2 wt% MOF Glass coating demonstrated nearly the same performances as that of the 5 wt% and 10 wt% MOF Glass coating samples. Considering the advantages of cost and energy density, we finally selected the sample with 2 wt% coating as the main samples. Therefore, unless otherwise specified, the Glass@Cathode (Glass@NCM-811, Glass@LRMO, and Glass@LCO) in this article refers to cathodes with 2 wt% MOF Glass coating.

Electrodes preparation

Generally, 1.0 g Glass@NCM-811, Glass@LRMO, and Glass@LCO powders were mixed with Carbon black (Dodochem Co,. Ltd.) and polyvinylidene fluoride (PVDF, Aladdin Scientific Corp.) powder in a ratio of 8:1:1 and then directly stirring in 1-Methyl-2-pyrrolidone (NMP, Sigma-Aldrich) for 4 hours to get a viscous solution, respectively. For comparisons, uncoated cathodes (bare NCM-811, LRMO and LCO) were also fabricated following the same processes. MOF Glass electrode was prepared by mixing MOF Glass, Carbon black and PVDF in a ratio of 8:1:1. Carbon black electrode was prepared by mixing Carbon black and PVDF in a ratio of 9:1. The obtained slurry was then homogeneously coated onto Al foil current collector by a scraper. After tiny pressing procedure, the active materials-loaded Al foil was vacuum dried at 110 °C overnight. The mass loading of the cathodes used for coin-cells was about 7.0 mg/cm^2 (corresponding to NCM-811, LRMO and LCO, electrode size: 12 mm in diameter), the mass loading of the Glass@NCM-811 cathode materials was about 31.8 mg/cm^2 for pouch-cell fabrication (to improve the energy density of pouch-cell, the ratio between Glass@NCM-811, carbon black and PVDF was 9:0.5:0.5, corresponding to 28.0 mg/cm^2 NCM-811). It is worth noting that for Li||Glass@NCM-811, Li||Glass@LRMO, and Li||Glass@LCO half-cell, thick unlimited lithium metal (400 μm Li) was used as anode, while for the Li||Glass@NCM-811 pouch-cell, thin limited lithium metal (negative to positive areal capacity equals to 3.89:1, N/P ratio ~ 3.9:1) was used as anode.

Cell assembly and electrochemical measurements

CR2032 coin cells were assembled in an argon-filled glove box, in which both the moisture and oxygen contents were controlled to be less than 1 ppm. Glass@NCM-811, Glass@LRMO, Glass@LCO, MOF Glass electrode and Carbon black electrode were employed as cathodes, Celgard 2500 (purchased from Neware) as separators (18 mm in diameter for coin-cells, 4.5 × 9.5 cm^2 for pouch-cells), and lithium foils were employed as anodes. For comparisons, bare NCM-811, LRMO and LCO were also coupled with lithium metals to fabricate coin-cells. Typical carbonate electrolyte (1 mol/L $LiFP_6$-EC/DMC, 60 μL, Dodochem Co,. Ltd.) was used for all those coin-cells. For Li||Glass@NCM-811 pouch-cell assembling, 2.6 g liquid typical electrolyte (corresponding to an low E/C ratio of 1.3 g Ah^{-1}) was added. The low E/C ratio can be ascribed to the greatly suppressed electrolyte decomposition. The Li||Glass@NCM-811 coin-cells and bare Li||NCM-811 coin-cells were operated with a potential limit between: 2.7-4.4 V, 2.7-4.6 V, respectively (defined 1 C = 220 mA/g, for NCM-811 based battery). The Li||Glass@LRMO coin-cell and bare Li||LRMO coin-cell were operated with a potential limit between 2.0-4.8 V (defined 1 C = 280 mA/g, for LRMO based cells). The Li||Glass@LCO coin-cells and bare Li||LCO coin-cells were operated with a potential limit between 3.0-4.6 V (defined 1 C = 220 mA/g, for LCO based cells). The Li||Glass@NCM-811 pouch-cell was measured under a potential limit between: 2.7-4.4 V. It worth noting that the prepared Li||Glass@NCM-811 pouch-cell was measured under external pressure. Enclosure for applying stack pressure, pouch cells are uniaxially constrained in a steel enclosure with an adjustable wall which can be tightened to apply varying uniaxial pressures (the stack pressure was about 10 MPa). Glass@NCM-811 cathode material immersed in water after 7 days was also coupled with Li metal to fabricate Li||Glass@NCM-811 coin-cell following the afore-discussed process to evaluate the water stability of the Glass@NCM-811 cathode material. The bare Li||NCM-811 battery with MOF Glass directly coated on the cathode electrode (defined as Li||Glass-NCM-811) was also assembled and test for comparison. The state of charge (SoC) vs. time plots of cells were collected at a CC charging rate of 6 C, followed by CV charging with a 0.2 C cut-off current. Rates performances of both Li||Glass@NCM-811 coin-cell and bare Li||NCM-811 coin-cell were measured under 2.7-4.4 V for 100 cycles (from 0.1 C to 5 C). After the rate performance test, GITT measurements were then conducted after 100th cycle of rate performance cycling between 3.0 and 4.4 V (versus Li/Li$^+$) with a titration step at 0.5 C of 8 min and a relaxation step of 1 h. Before each electrochemical characterization, the cells were kept on open circuit for 16 hours. All the potentials in this study were referenced to Li/Li$^+$. The galvanostatic electrochemical measurements were carried out under potential control using the battery tester system HJ1001SD8 (Hokuto Denko) at room temperature (25 °C in a climatic chamber). For the EIS tests, the electrochemical experiments were carried out under the control of a potentiostat (Potentiostat/Galvanostat PGSTAT30, Autolab Co. Ltd., Netherlands). Nickel-containing electrolytes were prepared by dissolving 400 ppm $Ni(TFSI)_2$ salt (Sigma-Aldrich) in the base electrolyte (1 M $LiPF_6$-EC/DMC). Li||Li symmetric cells were assembled in the glove box with 60 μL of the prepared electrolyte for each cell. Galvanostatic cycling was performed on a symmetric Li||Li cell at a Li plating/stripping current density of 1.0 mA cm^{-2} with a cycling capacity of 1.0 mAh cm^{-2} (1 h for each step). It should be noted that in order to obtain more accurate results, at least 8-10 batteries (fabricated and measured following the same procedure) were tested in one electrochemical experiment, and the data finally reported in this study were selected from the average performance of these batteries.

Morphology and structure characterization

SEM, TEM and XRD characterizations. The morphology of the as-prepared Zn-P-dmbIm MOF powder, MOF Glass, bare NCM-811 cathode material, Glass@NCM-811 cathode material, and the corresponding cycled bare NCM-811 cathode material, Glass@NCM-811 cathode material, cycled Li anodes were characterized with scanning electron microscopy (SEM, JEOL JSM-6380LV FE-SEM), focused ion beam scanning electron microscopy (FIB-SEM, TESCAN-AMBER) and high-resolution transmission electron microscopy (HR-TEM, ARM300, JEOL). X-ray diffraction (XRD) measurements were performed on a Bruker D8 Advanced diffractometer fitted with Cu-Kα X-rays (λ = 1.5406 Å) radiation at a scan rate of 0.016 °/s to investigate the structure information of the as-prepared Zn-P-dmbIm MOF powder, MOF Glass, bare NCM-811 cathode material, Glass@NCM-811 cathode material, and the corresponding cycled bare NCM-811 cathode material, Glass@NCM-811 cathode materials. For the pre-treatment procedures: The cycled cells were transferred into an Ar glove box once the electrochemical treatments were finished, and the electrodes were extracted from the cell and placed in a glass bottle. The electrodes were twice rinsed by dimethoxyethane (DME, Sigma Aldrich, 99%) to wash off the electrolyte salt and the residual solvent, and then evaporated in a vacuum chamber, connected to the glove box, for 12 hours. Note that, in order to restrain the exposure time to the ambient, samples (cycled electrodes) were tightly sealed into a glass bottle (fill with Ar gas), and transferred to the related chambers (SEM) as quickly as possible. Thus, we assumed the morphology and the component of electrode surface would not obviously change for such a short time exposure to the open air. FIB-SEM (TESCAN-AMBER) was also used to characterize the inside morphology of the cycled NCM-811 and cycled Glass@NCM-811 cathodes. HR-TEM (ARM300, JEOL) was conducted at 150 and 300 keV to collect scanning transmission electron microscopy images of Zn-P-dmbIm MOF powder, MOF Glass, bare NCM-811 cathodes, Glass@NCM-811 cathodes, and the corresponding cycled bare NCM-811 cathodes, Glass@NCM-811 cathodes for the atomic and structural analysis. The corresponding SEM/TEM EDS mapping of the cycled cathodes were also recorded.

Differential scanning calorimetry (DSC) measurement. DSC of Zn-P-dmbIm powder was carried out on a thermal analyzer (NETZSCH, STA 409) from 30 to 300 °C at the rate of 5 °C min^{-1} under dry flow of Ar.

Positron annihilation lifetime spectroscopy (PALS). The pore size of Zn-P-dmbIm MOF powder and the corresponding MOF Glass was

estimated by PALS. The Zn-P-dmbIm MOF powder was pelleted into a cylinder with a radius of 1.5 cm and thickness of ~1 mm, and the MOF Glass film was larger than 1 × 1 cm^2 square with a thickness of ~1 mm. The source of positrons was provided by ^{22}Na. The PALS measurements were carried out at 25 °C and the experimental data were analyzed by a four-finite lifetime component using LT 9.0.

FTIR characterizations. Attenuated Total Reflection Fourier-transform Infrared (ATR-FTIR) Characterization for Typical Electrolyte and Electrolyte Inside MOF Glass

ATR-FTIR measurements were carried out on a FT/IR-6200 spectrometer (JASCO Corp.) coupled with Platinum Diamond ATR, which consists of a diamond disc as an internal reflection element. The typical electrolyte (1 M $LiPF_6$-EC/DMC) and cycled Glass@NCM-811 cathode with thick MOF Glass coating (weight ratio of MOF Glass and NCM-811 was about 1:1) were placed on the ATR crystal. Then the spectrum was recorded to detect the liquid electrolyte peaks of typical electrolyte. The washed cycled Glass@NCM-811 cathode was attached on the plate of O_2 plasma etching instrument. By etching away the surface MOF Glass layer (etching for two times, about 5 nm), we detected the electrolyte information inside the MOF Glass by using the ATR-FTIR measurement.

Raman characterizations of electrolyte inside MOF glass and diluent (0.5 M), normal (1.0 M) and saturated $LiPF_6$-EC/DMC electrolyte. Liquid electrolytes under different concentrations (0.5 M, 1.0 M and saturated $LiPF_6$-EC/DMC electrolyte) were prepared for Raman measurement. The Raman spectra were recorded using a JASCO microscope spectrometer (NRS-1000DT). Electrolyte inside MOF Glass layer was also recorded following the same procedure as discussed in the ATR-FTIR test towards electrolyte inside MOF Glass layer.

Depth-resolution etching FTIR characterization for cycled NCM-811 and glass@NCM-811 cathode. For pretreatment, the cycled cells were transferred into an Ar glove box once the discharge finished, and the cathodes were extracted from the cell and twice rinsed by dimethoxyethane (DME, Sigma Aldrich, 99%) to wash off the electrolyte salt and the residual solvent, and then evaporated in a vacuum chamber, connected to the glove box, for ~15 min. The washed cycled cathodes were attached on the plate of O_2 plasma etching instrument. And the FTIR spectra were collected after each etching process. As a result, 10 points were recorded. The cycled bare NCM-811 cathode and the cycled Glass@NCM-811 cathode were tested using the etching FTIR following the aforementioned experiment processes.

Depth-resolution etching X-ray photoelectron spectroscopy (XPS) characterization. XPS measurement was performed using a VG scientific ESCALAB 250 spectrometers with monochromic Al Kα Ka source (1486.6 eV) under high vacuum. Similarly, to prevent long-time exposure to air environment, the samples (after rinsing and dry) were tightly sealed into an Ar-filled bottle and then soon transferred into XPS chamber as quickly as possible. The XPS was equipped with etching with different depth to analysis the component distribution.

Nuclear magnetic resonance (NMR) spectroscopy characterizations. The NMR spectra were recorded using a spectrophotometer (500 MHz Ultra-ShieldTM, Bruker). Typically, 256/128 (^1H/^{19}F) times were accumulated for one spectrum. The electrodes and separators were extracted from the cycled cells without further pretreatment. 750 μL of D_2O (99.9 atom % D, Sigma Aldrich) was used to extract the residual electrolyte and soluble parasitic products (mainly carboxylates and fluorides) from the electrodes and the separators, then the solution was transferred to septa-sealed NMR tube. To quantify the number of related components, 1 μL of benzene (C_6H_6, Sigma Aldrich, 99%) and 1 μL of fluorobenzene (C_6H_5F, Sigma Aldrich, 99%) were mixed and injected through the septa and employed as an internal standard. The method here was very similar as the ones introduced in our previous works.

Inductively coupled plasma-optical emission (ICP-OES) spectrometry characterizations. ICP-OES (optical emission spectroscopy) results were recorded using Thermo Scientific iCAP 5600 and PerkinElmer Optima 4300 DV. Metal dissolutions from cycled batteries were quantitatively confirmed measuring the Mn, Co and Ni-ion concentrations both in the electrolyte solutions and on the lithium-metal anode. The cycled separators (infiltrated by cycled electrolyte solutions) and lithium electrodes were bathed in DME solvent for 4 hours aging. The separator was salvaged out then the DME solution and Li anode were mixed with a mixture of concentrated hydrochloric acid and nitric acid mixture (3:1 in volume ratio). The solution was heated in a microwave for 2 hours (150 °C).

In-situ differential electrochemical mass spectrometry (In-situ DEMS) measurements. In-situ DEMS analysis was conducted to monitor gases generated during the initial charge process. NCM-811 and Glass@NCM-811 cathodes (22 mm diameter, prepared as described in the Electrode Preparation section, ~8 mg/cm^2 NCM-811 mass loading) were used with 1 mol/L $LiPF_6$-EC/DMC electrolyte (150 μL per cell) and glass fiber separators (Whatman GF/D). The electrodes were assembled into Swagelok-type cells with metallic lithium as the counter and reference electrode. The Swagelok-type cells were connected to a mass spectrometer, continuously purged with argon, which carried evolved gases for MS analysis. In-situ DEMS cell operation was performed using a VSP electrochemical workstation (Biologic), with mass signals recorded as a function of time and cell voltage. Temporal resolution of ion current intensity was optimized by selectively scanning m/z 32 and 44 signals.

Data availability

The data generated in this study are provided in the Supplementary Information/Source Data file. Source data are provided with this paper.

References

1. Tarascon, J. & Armand, M. Issues and challenges facing rechargeable lithium batteries. *Nature* **414**, 359–367 (2001).
2. Armand, M. & Tarascon, J. M. Building better batteries. *Nature* **451**, 652–657 (2008).
3. Etacheri, V., Marom, R., Elazari, R., Salitra, G. & Aurbach, D. Challenges in the development of advanced Li-ion batteries: a review. *Energy Environ. Sci.* **4**, 3243–3262 (2011).
4. Goodenough, J. B. & Kim, Y. Challenges for Rechargeable Li Batteries. *Chem. Mater.* **22**, 587–603 (2010).
5. Wang, G., Zhang, L. & Zhang, J. A review of electrode materials for electrochemical supercapacitors. *Chem. Soc. Rev.* **41**, 797–828 (2012).
6. Li, W., Erickson, E. M. & Manthiram, A. High-nickel layered oxide cathodes for lithium-based automotive batteries. *Nat. Energy* **5**, 26–34 (2020).
7. Xue, W. et al. Ultra-high-voltage Ni-rich layered cathodes in practical Li metal batteries enabled by a sulfonamide-based electrolyte. *Nat. Energy* **6**, 495–505 (2021).
8. Xue, W. et al. FSI-inspired solvent and "full fluorosulfonyl" electrolyte for 4 V class lithium-metal batteries. *Energy Environ. Sci.* **13**, 212–220 (2020).
9. Liu, Y., Zhu, Y. & Cui, Y. Challenges and opportunities towards fast-charging battery materials. *Nat. Energy* **4**, 540–550 (2019).
10. Niu, C. et al. Balancing interfacial reactions to achieve long cycle life in high-energy lithium metal batteries. *Nat. Energy* **6**, 723–732 (2021).
11. Niu, C. et al. High-energy lithium metal pouch cells with limited anode swelling and long stable cycles. *Nat. Energy* **4**, 551–559 (2019).

12. Fan, X. et al. Non-flammable electrolyte enables Li-metal batteries with aggressive cathode chemistries. *Nat. Nanotechnol.* **13**, 715–722 (2018).
13. Cao, X. et al. Monolithic solid–electrolyte interphases formed in fluorinated orthoformate-based electrolytes minimize Li depletion and pulverization. *Nat. Energy* **4**, 796–805 (2019).
14. Liu, D. et al. Atomically dispersed platinum supported on curved carbon supports for efficient electrocatalytic hydrogen evolution. *Nat. Energy* **4**, 512–518 (2019).
15. Li, J. et al. Structural origin of the high-voltage instability of lithium cobalt oxide. *Nat. Nanotechnol.* **16**, 599–605 (2021).
16. Yu, Z. et al. Molecular design for electrolyte solvents enabling energy-dense and long-cycling lithium metal batteries. *Nat. Energy* **5**, 526–533 (2020).
17. Shadike, Z. et al. Identification of LiH and nanocrystalline LiF in the solid–electrolyte interphase of lithium metal anodes. *Nat. Nanotechnol.* **16**, 549–554 (2021).
18. Yan, P. et al. Coupling of electrochemically triggered thermal and mechanical effects to aggravate failure in a layered cathode. *Nat. Commun.* **9**, 2437 (2018).
19. Liu, T. et al. Understanding Co roles towards developing Co-free Ni-rich cathodes for rechargeable batteries. *Nat. energy* **6**, 277–286 (2021).
20. Zhang, J. et al. Multifunctional solvent molecule design enables high-voltage Li-ion batteries. *Nat. Commun.* **14**, 2211 (2023).
21. Xie, Q., Li, W. & Manthiram, A. A Mg-doped high-nickel layered oxide cathode enabling safer, high-energy-density Li-ion batteries. *Chem. Mater.* **31**, 938–946 (2019).
22. Schipper, F. et al. From surface ZrO_2 coating to bulk Zr doping by high temperature annealing of nickel-rich lithiated oxides and their enhanced electrochemical performance in lithium ion batteries. *Adv. Energy Mater.* **8**, 1701682 (2018).
23. Kim, J. et al. A highly stabilized nickel-rich cathode material by nanoscale epitaxy control for high-energy lithium-ion batteries. *Energy Environ. Sci.* **11**, 1449–1459 (2018).
24. Zhang, S.-D. et al. Surface engineering of $LiCoO_2$ by a multifunctional nanoshell for stable 4.6 V electrochemical performance. *Energy Storage Mater.* **57**, 289–298 (2023).
25. Cui, C. et al. Structure and interface design enable stable Li-rich cathode. *J. Am. Chem. Soc.* **142**, 8918–8927 (2020).
26. Fan, X. et al. Crack-free single-crystalline Ni-rich layered NCM cathode enable superior cycling performance of lithium-ion batteries. *Nano Energy* **70**, 104450 (2020).
27. Lu, J. et al. Microstructures of layered Ni-rich cathodes for lithium-ion batteries. *Chem. Soc. Rev.* **53**, 4707–4740 (2024).
28. Fan, X. et al. All-temperature batteries enabled by fluorinated electrolytes with non-polar solvents. *Nat. Energy* **4**, 882–890 (2019).
29. Fan, X. & Wang, C. High-voltage liquid electrolytes for Li batteries: progress and perspectives. *Chem. Soc. Rev.* **50**, 10486–10566 (2021).
30. Lu, D. et al. Ligand-channel-enabled ultrafast Li-ion conduction. *Nature* **627**, 101–107 (2024).
31. Jie, Y. et al. Progress and Perspectives on the Development of Pouch-Type Lithium Metal. *Batteries. Angew. Chem. Int. Ed.* **136**, e202307802 (2024).
32. Lu, S.-Q. et al. Surface lattice modulation through chemical delithiation toward a stable nickel-rich layered oxide cathode. *J. Am. Chem. Soc.* **145**, 7397–7407 (2023).
33. Yu, H. et al. Surface enrichment and diffusion enabling gradient-doping and coating of Ni-rich cathode toward Li-ion batteries. *Nat. Commun.* **12**, 4564 (2021).
34. Liu, J. et al. Tuning Interphase Chemistry to Stabilize High-Voltage $LiCoO_2$ Cathode Material via Spinel Coating. *Angew. Chem. Int. Ed.* **61**, e202207000 (2022).
35. Ding, X. et al. An ultra-long-life lithium-rich $Li_{1.2}Mn_{0.6}Ni_{0.2}O_2$ cathode by three-in-one surface modification for lithium-ion batteries. *Angew. Chem. Int. Ed.* **59**, 7778–7782 (2020).
36. Bao, W. et al. Simultaneous enhancement of interfacial stability and kinetics of single-crystal $LiNi_{0.6}Mn_{0.2}Co_{0.2}O_2$ through optimized surface coating and doping. *Nano Lett.* **20**, 8832–8840 (2020).
37. Xu, G.-L. et al. Building ultraconformal protective layers on both secondary and primary particles of layered lithium transition metal oxide cathodes. *Nat. Energy* **4**, 484–494 (2019).
38. Yoon, M. et al. Reactive boride infusion stabilizes Ni-rich cathodes for lithium-ion batteries. *Nat. Energy* **6**, 362–371 (2021).
39. Chang, Z. et al. A liquid electrolyte with de-solvated lithium ions for lithium-metal battery. *Joule* **4**, 1776–1789 (2020).
40. Feng, Y. et al. Achieving high-power and dendrite-free lithium metal anodes via interfacial ion-transport-rectifying pump. *Adv. Energy Mater.* **13**, 2203912 (2023).
41. Xu, Y. et al. Ion-transport-rectifying layer enables Li-metal batteries with high energy density. *Matter* **3**, 1685–1700 (2020).
42. Chang, Z. et al. Tailoring the solvation sheath of cations by constructing electrode front-faces for rechargeable batteries. *Adv. Mater.* **34**, 2201339 (2022).
43. Xuan, X., Wang, J. & Wang, H. Theoretical insights into PF6− and its alkali metal ion pairs: geometries and vibrational frequencies. *Electrochim. Acta* **50**, 4196–4201 (2005).
44. Li, J. et al. Coordination Polymer Glasses with Lava and Healing Ability for High-Performance Gas Sieving. *Angew. Chem. Int. Ed.* **133**, 21474–21479 (2021).
45. Marino, C., El Kazzi, M., Berg, E., He, M. & Villevieille, C. Interface and safety properties of phosphorus-based negative electrodes in Li-ion batteries. *Chem. Mater.* **29**, 7151–7158 (2017).
46. Tu, S. et al. Fast-charging capability of graphite-based lithium-ion batteries enabled by Li_3P-based crystalline solid–electrolyte interphase. *Nat. Energy* **8**, 1365–1374 (2023).
47. Duan, Y. et al. Insights into Li/Ni ordering and surface reconstruction during synthesis of Ni-rich layered oxides. *J. Mater. Chem. A* **7**, 513–519 (2019).
48. Feng, Z. et al. A Three in One Strategy to Achieve Zirconium Doping, Boron Doping, and Interfacial Coating for Stable $LiNi_{0.8}Co_{0.1}Mn_{0.1}O_2$ Cathode. *Adv. Sci.* **8**, 2001809 (2020).
49. Yan, J. et al. Encapsulation of nano-Si into MOF glass to enhance lithium-ion battery anode performances. *Nano Energy* **103**, 107779 (2022).
50. Gao, C. et al. Metal-Organic Framework Glass Anode with an Exceptional Cycling-Induced Capacity Enhancement for Lithium-Ion Batteries. *Adv. Mater.* **34**, 2110048 (2022).
51. Liu, S. et al. Vitrified Metal–Organic Framework Composite Electrolyte Enabling Dendrite-Free and Long-Lifespan Solid-State Lithium Metal Batteries. *ACS Nano* **18**, 14907–14916 (2024).
52. Xiang, Y. et al. Continuous Amorphous Metal–Organic Frameworks Layer Boosts the Performance of Metal Anodes. *ACS Nano* **17**, 19275–19287 (2023).

Acknowledgements

This work was supported by the National Key R&D Program of China (2024YFB3814200), National Natural Science Foundation of China (grant no. 92372201, 22209208), NSF of China (grant no. U1801251).

Author contributions

Z.C. and H.Z. contributed to the design of the research. L.B. and Y.X. performed the experimental data analysis. L.B. and Y.X. conducted the electrochemical and spectroscopic characterizations. Y.X., Y.L., D.Z. performed the SEM and the XRD characterizations. Y.L., S.Z. and W.Y. helped with the XPS, ATR-FTIR/Etching FTIR and other measurements related to the physicochemical properties of separators. All authors co-wrote the manuscript. Z.C. and H.Z. supervised the work. All authors discussed the results and commented on the manuscript.

Competing interests
The authors declare no competing interests.

Additional information
Supplementary information The online version contains supplementary material available at https://doi.org/10.1038/s41467-025-58639-z.

Correspondence and requests for materials should be addressed to Zhi Chang or Haoshen Zhou.

Peer review information *Nature Communications* thanks the anonymous reviewers for their contribution to the peer review of this work.